Soft Matter

PAPER

View Article Online
View Journal | View Issue

Cite this: *Soft Matter*, 2024, **20**, 5538

Aluminosilicate colloidal gels: from the early age to the precipitation of zeolites†

Arnaud Poulesquen, *[a] Donatien Gomes Rodrigues,[b] Bavand Keshavarz,[c] Nicolas Courtois,[a] Jan Ilavsky[d] and Gareth H. McKinley[e]

Aluminosilicate hydrogels are often considered to be precursors for the crystallisation of zeolites carried out under hydrothermal conditions. The preparation of mechanically homogeneous aluminosilicate gels enables the study of these materials through bulk rheology and observation of the aging dynamics until the precipitation of crystalline zeolites. The first part of this study deals with the establishment of ternary state diagrams, in order to identify the range of chemical formulations that enable preparation of single-phase homogeneous gels. Then, by studying the viscoelastic moduli during the gelation reaction, and by yielding the gel under large deformation, we propose an empirical law considering the partial order of reaction on each chemical element, to predict the gelation time according to the chemical formulation. The scaling behavior of the elastic properties of this colloidal gel shows a transition from a strong link behavior to a weak link regime. Long term aging results in the shrinkage of the gel, accompanied by syneresis of interstitial liquid at the surface. Zeolites precipitate through crystallisation by a particle attachment mechanism, when thermodynamic equilibrium is reached. The stoichiometry of the precipitated zeolites is not only consistent with the concentration of the remaining species in the supernatant but, surprisingly, it is also very close to the partial order of the reaction of the chemical elements involved in the determination of the critical gel point. This indicates a strong correlation between the morphology of the soft amorphous gel network that is formed at an early age and those of the final solid precipitated crystals.

Received 6th February 2024,
Accepted 15th June 2024

DOI: 10.1039/d4sm00181h

rsc.li/soft-matter-journal

1 Introduction

Aluminosilicate-based materials, such as synthetic zeolites or alkali activated materials (AAM), also referred to as geopolymers, have many applications in various areas such as catalysis or adsorption processes for separation,[1,2] construction materials,[3,4] wastewater treatment by ionic exchange processes,[5,6] soil stabilization by grouting[7,8] as well as in the nuclear industry.[9–13] For both classes of materials, the synthesis process relies on polycondensation reactions that occur in the molecular scale between alkali silicate and aluminate species in solution.[14–16] In the case of geopolymers, the aluminates emerge from the slow dissolution of aluminosilicate precursors as metakaolin,[17] fly ash or slags.[18,19] In the case of zeolite production, however, the aluminates are introduced directly into the alkali silicate solution, which initiates the fast reaction between silicate and aluminate groups due to the very high reactivity between the two species.[16,20,21] Although both classes of alumino-silicate-based materials are synthesized with the same chemical elements (Si, Al, Na and H_2O), there are two major differences between them. Firstly, the reaction mixture differs between these two materials. Indeed, in contrast to the synthesis of geopolymer binders,[22] a high water content and limited alkalinity are necessary for the production of zeolites. Secondly, zeolite-type materials are usually synthesized under *hydrothermal conditions* which commonly refers to a range of techniques for crystallizing substances from high-temperature aqueous solutions at high vapor pressures that can be considered as a "black box", whereas AAM or geopolymers are often produced at room temperature. For zeolites, the resulting solid material consists of a powdered crystalline structure made of silicon, aluminum and oxygen that form a highly structured framework with cavities and nanochannels through which cations, water and/or small molecules may be transported through.[1] On the other hand, geopolymers are

[a] *CEA, DES, ISEC, DPME, Univ. Montpellier, F-30207 Bagnols-sur-Cèze, France. E-mail: arnaud.poulesquen@cea.fr*
[b] *CEA, DES, ISEC, DMRC, Univ. Montpellier, F-30207 Bagnols-sur-Cèze, France*
[c] *Department of Mechanical Engineering and Materials Science, Duke University, Durham, NC, USA*
[d] *Advanced Photon Source, Argonne National Laboratory, Lemont, Illinois 60439, USA*
[e] *Hatsopoulos Microfluids Laboratory, Department of Mechanical Engineering, Massachusetts Institute of Technology, Cambridge, Massachusetts 02139, USA*

† Electronic supplementary information (ESI) available. See DOI: https://doi.org/10.1039/d4sm00181h

micro–meso–macroporous monolithic amorphous materials, with a framework composed of SiO_4 and AlO_4 tetrahedra.[23] A cation (often Na and/or K) compensates for the charge deficiency of aluminum atoms and the porosity is fully saturated with highly concentrated pore water, triggering the ionic exchange process. They are considered to be zeolite precursors due to the fact that at room temperature they are in a metastable state but they can ultimately be crystallized into zeolitic structures if heated at high temperature.[24]

Before their transformation to solid materials (powder or monolith for zeolites and geopolymers, respectively), the evolution of their viscoelastic properties may be monitored as a function of time. For geopolymers, the viscoelastic moduli slowly increase over a few hours, until the gelation time is reached and the material turns into a viscoelastic solid with an elastic modulus around a few MPa.[25,26] In the case of hydrogels, also considered as amorphous precursors of zeolites, the kinetics of gelation is faster (shorter than one hour) and the elastic modulus only ranges from a few Pa to a few kPa.[16,27,28]

Most synthetic zeolites are usually formed in basic media (mainly with hydroxide ions as the mineralizing agent) using alkali and/or tetra-alkylamonium cations as a structure-directing agent,[29] with the exception of some recent studies where zeolite precipitation has been extended into acidic media.[30] As pointed out in the review by Valtchev *et al.*,[21] depending on the specific details of the chemical formulation (such as the Si/Al ratio, the concentration of alkali cation and the water content), the zeolites formed may vary from ultra-dense gels and hydrogels to optically clear solutions. Although the hydrogel systems are complex due to their inhomogeneity, study of their rheomechanical properties is of particular importance due to their widespread use in the production of industrial zeolites.[31] Many studies have been dedicated to characterization of the gels, with direct observations by high resolution transmission electron microscopy (HRTEM), scanning electron microscopy (SEM), transmission electron microscopy (TEM)[31–34] and *in situ* atomic force microscopy (AFM).[35,36] These studies have been used to image the evolution of the amorphous gel over time, until the ultimate state involving crystallisation and growth of the zeolites. Spectroscopic techniques such as Fourier transform infrared (FTIR),[34] and[27] Al or[29] Si nuclear resonance magnetic (NMR),[27,28,37–39] are also very useful for identifying the connectivity of the spatial framework and the structure of the aluminosilicate generated (*e.g.* the coordination of silicon and aluminum atoms) in the solid network. In basic media, tetrahedral TO_4 networks where T = Si or Al derived from the polycondensation of soluble species in the mixture constitute the spatial framework of the growing zeolites. Time-resolved scattering techniques using neutrons or X-rays offer the advantage of probing *in situ* the structural evolution at mesoscales in a non-invasive manner. Complementary to direct visualisation, scattering has been widely utilized to study colloids suspended in a clear sol[40–44] or in hydrogel systems.[16,28] Obviously, structural parameters such as the size of the primary aluminosilicate particles, the cluster size and the fractal dimension of such aggregates strongly depend on the chemical formulation of the initial ingredients and parameters such as the Si/Al ratio, aluminum concentration, water content, and nature of the alkali cations as well as the conditions of synthesis such as temperature and relative humidity.

The selection of the starting materials and especially the silicon source can have a very pronounced impact on the formation mechanism of the final product. Indeed, if silica nanoparticles such as a Ludox colloidal suspension are used as precursors, an initial dissolution step occurs in alkaline media, releasing some silicate monomers or oligomers into the reactive mixture.[45] On contact with a source of alumina, polymerization is initiated between aluminate and silicate, forming a gel around the remaining undissolved silica particles, driving their aggregation into worm-like particles (WLPs).[46–48] In the case of an alkali silicate solution, also referred to as *waterglass*, the silicates are already dissolved and possess different degrees of connectivity, denoted Q_i (with i = 1 to 4), where the proportion of each constituent can be tuned with the alkali content.[49,50] The average connectivity of the Si centers decreases when the alkali hydroxide concentration increases, yielding smaller and more reactive species (with respect to the alumina source). In either of the two scenarios discussed above, an amorphous precursor is always observed before and throughout the nucleation of zeolites, leading to a two-step nucleation process, often referred to as a ''non-classical pathway'',[51] which is also observed in many other crystallisation processes.[52] Several mechanisms have been proposed to describe the induction period, such as aggregation, densification, formation of voids or appearance of an alkali-rich zone. Dynamical changes take place before and throughout the nucleation process,[21,33,42,43,46,51] but a global framework for zeolite synthesis is yet to be provided.

Our purpose in this paper is not to specifically study the nucleation and growth of the zeolites, but rather to provide new insights into the early stage processes occurring before the crystallisation of zeolites. Our main focus is on the rheological, structural and aging aspects of these hydrogels, as we vary the relative chemical composition of the building elements. To the best of our knowledge, there is a paucity of substantive studies on the effect of formulation changes on the developing rheological properties of homogeneous aluminosilicate hydrogels, with the exception of a few specific studies that are focused on geopolymer gels.[27,28]

Recently, we studied the rheology of aluminosilicate hydrogels[16] and showed that this class of aging materials can be considered to be weak colloidal physical gels in which the particles interact with each other *via* a potential well described by the DLVO (Derjaguin, Landau, Verwey and Overbeek) theory.[53] The characterization of these gels at the mesoscale using time-resolved SAXS and USAXS reveals that the kinetics of polycondensation are very fast, with initial consumption of dissolved silicate at high q (small length scale) resulting in rapid aluminsosilicate growth, reaching a size around 1 nm. These building units aggregate to form clusters with a fractal dimension around $2 \leq d_f \leq 2.1$, suggesting a reaction-limited cluster aggregation mechanism.[54] The Si/Al ratio is sufficiently

low, meaning that the aluminum content is sufficiently high (Si/Al $\approx$ 10 and [Al] = 0.12 mol l^{-1}) to produce a homogeneous hydrogel with an elastic modulus of a few kPa. Indeed, the volume fraction of particles ($\phi \approx$ 1–2%) is sufficient to form a space-spanning network whose strength depends on the chemical and physical nature of the underlying framework,[55,56] as we will examine in detail later in this paper.

From a mechanical characterisation point of view, the evolution of the viscoelastic parameters can also be monitored during gelation using novel time-resolved waveforms such as exponential chirps.[57] Using the concept of time-connectivity superposition we can generate a master curve of the mechanical response of these gels over 7–8 decades of frequency (or a similar range of corresponding timescales). These master curves for the dynamic mechanical properties and the evolving relaxation time spectrum of these gels reveal the dual nature of these materials; they exhibit both gel- and glass-like behaviors at large and small length- and time-scales, respectively. This behavior can be well described using a simple three-parameter model called the Fractional Maxwell Gel (FMG).[16,58] Another key finding from our previous study is the observation that the fractal structure of the nanoparticle gel is set at the critical gel point and these fractal remnants persist in the microstructure of the underlying network during the subsequent aging process. This resonates with the seminal observations of Martin and Adolf[59] in the context of chemically cross-linked gels that ''the structures formed at the gel point are not completely absent in the final gel'' and our findings show that similar principles apply to colloidal physical gels. This observation can also rationalize results from other studies such as the one by Valtchev and Tosheva,[21] in which the authors state that the initial polymerization reaction occurring at room temperature during the induction period predetermines, to a great extent, the reaction pathway followed during subsequent hydrothermal treatment. In the present work we first investigate the influence of the chemical composition on the formation of a homogeneous colloidal gel by exploring the corresponding ternary phase diagrams. We then discuss the temporal evolution of the linear viscoelastic properties *i.e.* the elastic storage modulus, $G'(\omega,t)$ and viscous loss modulus, $G''(\omega,t)$ during gelation of the aluminosilicate species. This is followed by a detailed discussion of the linear viscoelastic spectrum obtained in mature gels and the effects of nonlinear oscillatory tests with increasing strain amplitude that eventually lead to the destruction of the studied gels. The results are compared with appropriate theoretical models from the literature,[55] enabling us to connect the measured linear and nonlinear rheological properties to key structural parameters, such as the fractal dimension and the cluster size. We use the simple and compact fractional constitutive model to accurately capture the power-law viscoelastic behavior of these gels and also study the influence of the aluminum and sodium concentrations on the resulting mechanical response. Finally, by monitoring the volume occupied by the gel over time and analysing the composition of the solution that is exuded from it, we investigate the aging of the hydrogels at elevated temperatures (40 and 50 °C) over the period of a few weeks until the crystallisation of zeolites. The influence of the aluminum and sodium content on the structure of the final precipitated zeolites is analysed using structural characterization performed *via* X-ray diffraction (XRD).

2 Materials and methods

2.1 Chemical products

Commercial sodium silicate solution (Betol 39T, [Si] = 6.26 mol L^{-1}; [Na] = 3.64 mol L^{-1}) and sodium aluminate solution (Stabisil 19, [Al] = 5.89 mol L^{-1} [Na] = 9.44 mol L^{-1}) were provided by Woellner GmbH (Germany). Sodium hydroxide pellets (99%) were provided by Alfa Aesar. Each chemical product was used as received without further purification. Water was used after deionization using a Milli-Q Water purification system and was collected with a resistivity of about 18.2 MΩ cm.

2.2 Formulation of hydrogels

2.2.1 Preparation of precursors. The solutions of silicate and aluminate were prepared by dilution of commercial Betol 39T and Stabisil 19, respectively. Sodium hydroxide concentration was adjusted by adding solid NaOH pellets. In order to facilitate the solubilization of NaOH, it was first dissolved in a small amount of deionized water at room temperature. The solutions were left to cool down at room temperature. We then prepared two beakers by adding Betol in one or Stabisil in other, and both solutions were homogenized independently. The volume was then adjusted with water to reach the desired concentration of dissolved elements (Si, Al and Na).

2.2.2 Synthesis of aluminosilicate hydrogels. Aluminosilicate hydrogels were synthesized by isochoric addition of aluminate solution in silicate solution, in order to obtain a homogeneous gel by avoiding an excessively high reactivity, for our rheological characterization. Aluminates were quickly added into the silicate solution under vigorous stirring using an overhead stirrer equipped with a 3-bladed propeller at 700 rpm. After addition, the mixture was stirred for 5 seconds. The aluminosilicate solution was then left to stand until the formation of the hydrogel.

2.3 Rheological characterization

2.3.1 Rheological measurements. Rheological measurements were performed using an Anton-Paar MCR 302 rheometer, operating in the dynamic stress-controlled mode. We used a six-bladed vane geometry and a mixing bowl to perform *in situ* rheological measurements during mixing of aluminate and silicate solutions. We first added the silicate solution into the bowl while stirring it rapidly at a shear rate $\dot{\gamma} = 200\ s^{-1}$. After the addition of aluminate with a syringe, we stirred the mixture for another 30 seconds at the same shear rate (see Fig. S1 and S2 in the ESI,† for details of sequences and scheme). By adding hexadecane on top of the gelling solution and using a solvent trap we avoid drying of the samples. The experiments were primarily carried out at room temperature, except for a few tests

that were performed over a range of temperatures to enable estimation of the thermal activation energy.

After the pre-shear, we performed a time-sweep measurement in the linear regime and monitored the evolution of the storage (G') and loss (G'') moduli as a function of reaction time. This sequence was performed at fixed values of strain amplitude and frequency, γ_0 = 1% and $\omega = 4\pi$ rad s^{-1}, respectively. After observing the storage modulus approach a constant plateau value, we measured the linear dynamic response of the material using a frequency sweep test performed between 100 and 0.1 rad s^{-1} while maintaining a fixed strain amplitude of 1%. We then measured the nonlinear response of the material through a strain sweep at a fixed value of oscillation frequency ω = 1 rad s^{-1}. This enabled us to estimate the critical strain that separates the linear and non-linear response of the material.

2.3.2 Rheological model. To model the linear viscoelastic response of the studied gels, we use a Fractional Maxwell Gel (FMG) model.[16,58] This is a reduced subset of the more general Fractional Maxwell Model (FMM),[60] with a purely elastic gel-like response at high frequencies. This linear model can be written as a fractional differential equation between strain and stress:

$$\sigma + \frac{\mathbb{V}}{G_0}\frac{\mathrm{d}^\alpha \sigma}{\mathrm{d}t^\alpha} = \mathbb{V}\frac{\mathrm{d}^\alpha \gamma}{\mathrm{d}t^\alpha}, \tag{1}$$

where $\frac{\mathrm{d}^\alpha}{\mathrm{d}t^\alpha}$ represents the Caputo fractional derivative of order α.[16,60] This is a three parameter model, in which $\mathbb{V}$ represents a quasi-property (with dimension of Pa s$^\alpha$). As discussed by Keshavarz *et al.*,[16] $\mathbb{V}$ is a quasi-property that is very similar to the gel point strength that Winter and Chambon[61] have introduced in their rheological study of the gel point. A detailed discussion in Keshavarz *et al.*[16] shows that in the fractal network of an aging weak colloidal gel, such as aluminosilicate systems, $\mathbb{V}$ captures the dissipation level of the network at small length-scales $G''(\omega \to \infty) \approx \mathbb{V}\omega^{-\alpha}$ where a scale-free relaxation gives rise to a power-law viscoelastic behavior in the mechanical spectroscopy of these pasty materials. G_0 is the elastic modulus of the gel and $0 < \alpha \leq 1$ is a dimensionless power law exponent. In the limit of $\alpha \to 1$, this model reduces to the classical Maxwell model of linear viscoelasticity. Fourier transformation of eqn (1) yields the following expression for the complex viscoelastic modulus:

$$G^*(\omega) = G'(\omega) + iG''(\omega) = G_0\frac{(i\omega\tau)^\alpha}{1 + (i\omega\tau)^\alpha}, \tag{2}$$

where $\tau = (\mathbb{V}/G_0)^{1/\alpha}$ is a characteristic timescale for this model and G_0 is the plateau value of the elastic modulus at high frequencies. The storage and loss modulus of the weak colloidal gel are computed from the real and imaginary parts of the complex modulus and given by

$$\frac{G'(\omega)}{G_0} = \frac{(\omega\tau)^\alpha \cos(\pi\alpha/2) + (\omega\tau)^{2\alpha}}{(\omega\tau)^{2\alpha} + 2(\omega\tau)^\alpha \cos(\pi\alpha/2) + 1} \tag{3}$$

$$\frac{G''(\omega)}{G_0} = \frac{(\omega\tau)^\alpha \sin(\pi\alpha/2)}{(\omega\tau)^{2\alpha} + 2(\omega\tau)^\alpha \cos(\pi\alpha/2) + 1} \tag{4}$$

The characteristic timescale τ divides the viscoelastic response predicted by the model into two regions. At low frequencies, $\omega \ll 1/\tau$, the model predicts the power-law behavior for both storage and loss moduli $G'(\omega\tau \to 0) \sim G''(\omega\tau \to 0) \sim G_0(\omega\tau)^\alpha$, while at high oscillation frequencies $\omega \gg 1/\tau$, the elastic modulus approaches a plateau value of $G'(\omega\tau \gg 1) \sim G_0$ and the loss modulus decays to zero in a power-law manner, $G''(\omega\tau \gg 1) \sim \omega^{-\alpha}$.

2.4 X-ray measurement techniques

2.4.1 Ultra small, small and wide angle X-ray scattering (USAXS/SAXS/WAXS). USAXS/SAXS data for the mature gel were collected using the APS 9ID USAXS/SAXS/WAXS instrument.[62,63] The X-ray energy was 21 keV, and the data collection times were 90 seconds for USAXS and 30 seconds for SAXS. Data were fully background-corrected using the same measured container + solvent (water) scattering pattern, and placed on an absolute intensity scale using instrument-provided software.[62–64] Absolute intensity (in cm^{-1}) is plotted *versus* the magnitude of the scattering vector q:

$$q = \frac{4\pi}{\lambda}\cdot \sin\frac{\theta}{2} \tag{5}$$

where λ is the wavelength of incident radiation and θ is the scattering angle. USAXS data were de-smeared using established de-smearing routines.[65] USAXS and SAXS data were merged together, yielding data over about four decades in q space $10^{-4} \leq q \leq 1$ Å^{-1}.

2.4.2 X-ray diffraction (XRD). XRD data were collected using a PANalytical XPert Pro MPD diffractometer using Cu Kα radiation (λ = 1.54 Å) and the X'Celerator detector. The samples were scanned over 2θ angles spanning $5^\circ \leq 2\theta \leq 75^\circ$ for 40 min.

2.5 Scanning electron microscopy (SEM)

The observations were made on a Zeiss Supra 55 SEM at 15 keV, using backscattered electrons. EDS images and spectra were acquired using Esprit 1.9 software. The samples were metallized under vacuum with carbon, in order to avoid surface charging.

2.6 Inductively coupled plasma-optical emission spectrometry (ICP-OES)

The silicon and aluminum concentrations were measured by ICP-OES, using a Thermo Scientific iCAP 6000 Series device. The samples were diluted in 3% HNO_3 in order to reach an expected concentration around 10–15 mg L^{-1}. The maximum concentration of total elements in a sample should be below 1 g L^{-1}. External calibration with elemental standards of interest was performed from 0 to 20 mg L^{-1}.

3 Results and discussion

The formation of aluminosilicate species occurs instantaneously following addition of the sodium aluminate solution to the sodium silicate solution (see Fig. S1 and S2 in the ESI†). The aluminates formed in high alkaline media are in $[Al(OH)_4]^-$ monomer form. On the other hand, the silicate species may have various degrees of connectivity according to the nature and the concentration of the alkali cation (Me = sodium or potassium...). Indeed, it is known that a decrease of the Si/Me molar ratio (by increasing the alkali content Me and keeping the concentration of Si constant) entails a depolymerization of the silicate oligomers.[15,66–68] Recently, we have shown by molecular simulation and time-resolved X-ray scattering that the decondensation of silicate species is triggered by hydroxide ions that weaken and break the Si–O bonds, whereas silicate clusters are not impacted by water dilution, suggesting a protecting effect of the sodium cations with respect to the silicate chains.[50] The decondensation scenario is described by the well known chemical equilibrium (6).[69]

$$[\equiv Si-O-Si\equiv] + HO^- \rightleftharpoons \equiv Si-O^- + HO-Si\equiv \quad (6)$$

while hydroxide ions are consumed in decondensation of silicate bonds, aluminum acts as a bond former with respect to the silicate, as described by the chemical eqn (7).

$$[\equiv Si-OH] + [Al(OH)_4]^- \rightarrow \equiv[Si-O-Al(OH)_3]^- + H_2O \quad (7)$$

Consequently, the reactivity, the homogeneity, the physicochemical and the mechanical properties of the ensuring polymerized network depend not only on the overall chemical composition of the hydrogel but also on the way the gel is prepared as observed in Fig. 1. As previously mentioned, a gel is typically obtained after mixing alkali silicate and aluminate solutions in isovolumic proportion in order to avoid excessively high reactivity. The addition of sodium in the silicate or in the aluminate solution also has an impact on the kinetics of gelation of the hydrogel but not on the mechanical properties of the final gel (Fig. S3 in the ESI†). The presence of sodium hydroxide leads to decondensation of the silicate species, increasing their mobility and reactivity with respect to the aluminate. On the other hand, adding sodium hydroxide into the aluminate solution does not modify the speciation of aluminum and therefore the kinetics of gelation. The gel preparation protocol is thus crucial, because two concomitant but antagonist reactions take place when both solutions are mixed, *i.e.* the polymerization of aluminosilicate species and the breaking of silicate bonds, when an excess of alkali hydroxide (and particularly OH^-) is present in the aluminate solution.[16]

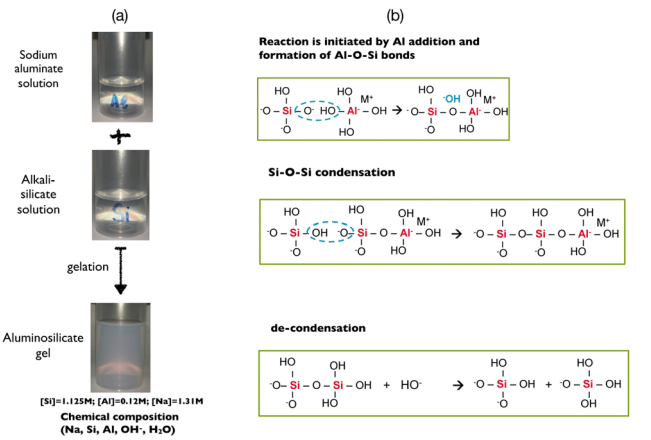

Fig. 1 (a) Pictures of the sodium aluminate solution and the sodium silicate solution before mixing and the resulting aluminosilicate gel after formation. (b) Reaction is initiated by introduction of aluminate and consequent formation of Al–O–Si bonds *via* a condensation reaction. In addition to these reactions, decondensation reactions can occur simultaneously due to a higher concentration of hydroxide ions.

3.1 Ternary phase diagrams

Ternary phase diagrams for silicate/aluminate/sodium hydroxide mixtures were determined for various water contents in order to identify optimal chemical compositions that enable synthesis of a homogeneous hydrogel (Fig. 2). After stirring, the solutions were allowed to rest for about one hour and visually inspected. The various amounts of silicate, aluminate and sodium are expressed in weight fraction (wt/wt), f_m, of SiO_2, Al_2O_3 and Na_2O (calculated from): $(m(i)/(m_{total} - m(H_2O)))$ and water amount expressed in wt% (calculated from): $(m(H_2O) \times 100/m_{total})$. The ternary phase diagrams shown in Fig. 2 with various delimiting zones were then obtained.

- Zone (I): monophasic liquid. For 80, 85, 90 and 95 wt% water content, the mixtures remain monophasic and clear. This zone was observed at the lowest amount of aluminate (approx. $f_m(Al_2O_3) < 0.05$ wt%) or silicates (approx. $f_m(SiO_2) < 0.05$ wt%) (blue hatched zone (I) in Fig. 2).
- Zone (II): precipitation of crystallized solid. A domain corresponding to the precipitation of white solid was observed (green square zone (II)). This was not observed for the composition containing 85 wt% water. Although silicate and aluminate are soluble in water, the solubility product of zeolites is very low. Šefčík *et al.* demonstrated the solubility product (K_{sp}) of zeolite-A was equal to 1.2×10^{-8} mol^3 L^{-3} for sodium concentrations ranging from 1 to 4 mol L^{-1}.[70]
- Zones (III), (IV) and (V): gel formation. In the case of the highest water content (95%), a few formulations allowed the formation of gel particles visible to the naked eye (orange hatched zone (III)). These gel particles settled down and formed a layer at the bottom of the container with a large excess of clear solution at the top. Because $f_m(Al_2O_3)$ was low (approx. 0.05 wt%) and the amount of water (95 wt%) was high, the amorphous particles could not percolate throughout the overall volume to produce a homogeneous hydrogel. For higher Al_2O_3 weight fractions, the turbidity of the mixture gradually increases until bulk percolation of the gel network (solid red zone (IV)). The gelation was progressive in time due to the reasonable reactivity rates in this range of composition. The time needed for total homogeneous gelation was measured to vary from a few minutes to a few hours according to the chemical formulation. However, in some cases,

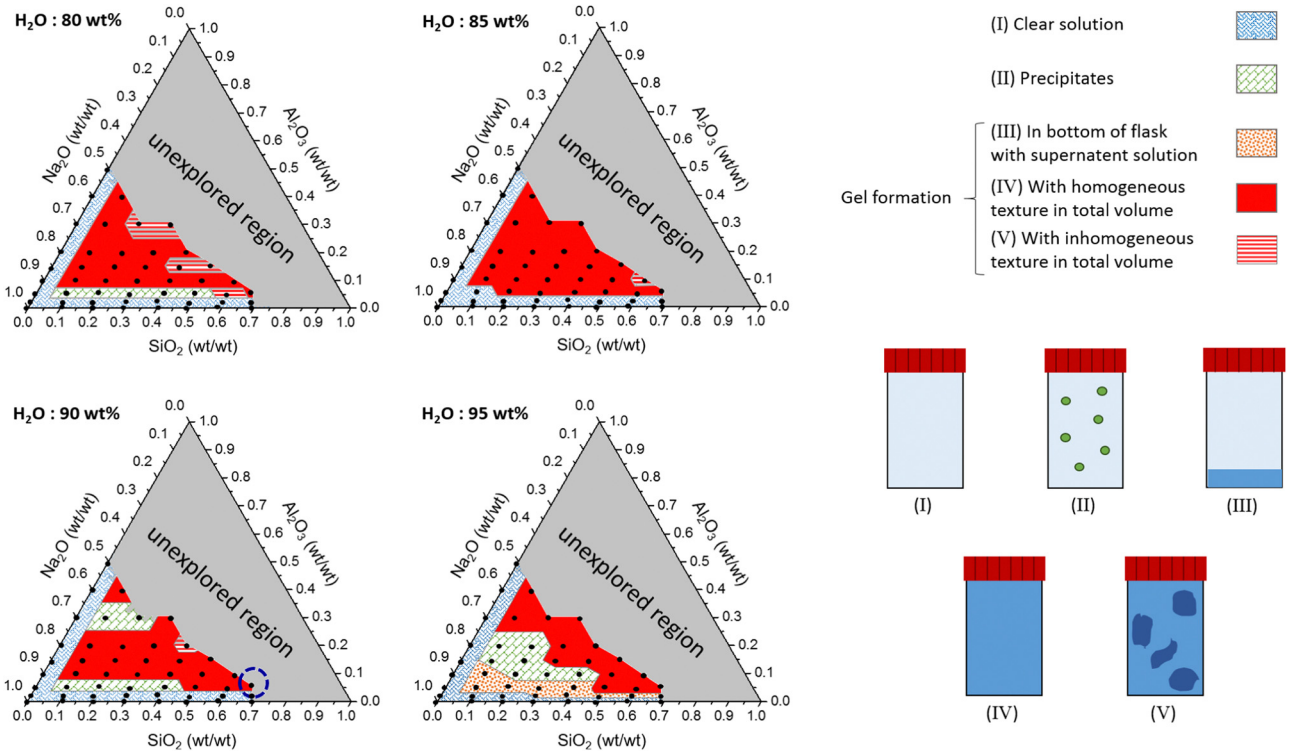

Fig. 2 Ternary state diagrams of $SiO_2/Al_2O_3/Na_2O$ formulations with total weight fractions of H_2O equal to 80, 85, 90 and 95 wt%. Grey regions correspond to unexplored regions. The dotted blue circle appearing in the 90 wt% of the water ternary phase diagram corresponds to the formulation studied in detail.

part of the gel was formed instantaneously and locally during addition of aluminate (red hatched zone (V)). The gelation of the remaining solution occurred a few minutes later when the aluminate monomers diffuse throughout the bulk to react with the silicate species. This two-stage gelation provides a very inhomogeneous gel and is mainly observed for the lowest water content (see Fig. S4 in the ESI†). On the other hand, increasing the water content reduces the reactivity between aluminate and silicate species entailing the vanishing of the zone (V) for H_2O = 95 wt%. It is therefore evident that the concentrations of reactive species and the preparation method have an impact on the homogeneity of the entire gel. At the molecular scale, the reaction kinetics between aluminate and silicate are very fast, leading to high reactivity. Therefore, diluting the two solutions in water before mixing them is recommended to prevent excessive reactivity. On the other hand, it is important to mention that, for the chemical formulations studied in this work, the gel phases remain unchanged, and it is clearly the reaction kinetics that control the system.

The grey zone corresponds to unexplored regions of the formulation space. Because of the fixed initial sodium concentration in the commercial alkali silicate (Betol) and alkali aluminate (Stabisil) solutions, a large region of the ternary diagram at low $f_m(Na_2O)$ could not be explored (grey zone). Carefully comparing the ternary diagrams highlights the observation that the more diluted the initial reactants are, the smaller the region of homogeneous gelation.

3.2 Influence of the chemical formulation on the gelation process

3.2.1 Time-resolved rheology. In order to obtain information about the gelation process and how it varies with chemical formulation, we first performed oscillatory rheology tests (time sweep) in the linear domain, to measure the temporal evolution of both the storage and loss moduli (Fig. 3). In the pre-gel state, the material is a viscoelastic liquid with a loss modulus that is larger than the elastic modulus and a phase angle, $\tan\delta = G''/G' > \pi/4$. During the gelation process, both moduli slowly grow in time until the material passes through a crossover point where $G' = G''$, after which the viscoelastic moduli both increase rapidly with time. The measured storage modulus exhibits faster temporal growth compared to the loss modulus and the gel becomes increasingly solid-like. The rate of increase in the elastic modulus ultimately reduces as the reactive species are consumed and we observe an approach to an asymptotic plateau value. However, the loss modulus $G''(\omega,t)$ passes through a local maximum, before slowly decreasing with time. This is characteristic of an aging soft glassy material.[71] In the next section, we will discuss the influence of chemical formulation on the gelation time t_{gel} that, for the sake of simplicity, we approximate here as the crossover point, *i.e.*, $G'(\omega_0, t_{gel}) = G''(\omega_0, t_{gel})$, where ω_0 is the fixed oscillatory test frequency used for the time sweep. A more precise determination of the gelation time can be performed using time-resolved mechanical spectroscopy of the gel during the gelation process but, as shown by Keshavarz *et al.*,[16] the crossover point is a good

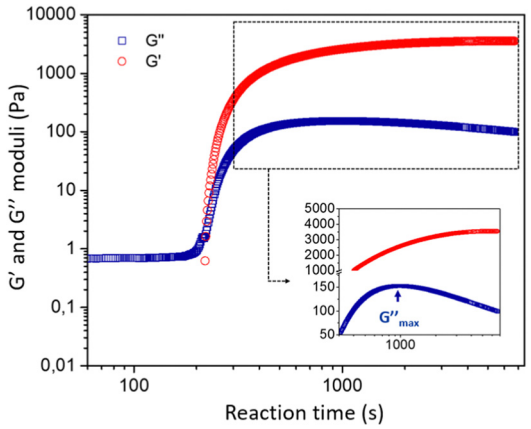

Fig. 3 Evolution of the linear viscoelastic moduli G' and G'' during the gelation process. Conditions: [Si] = 1.125 mol L^{-1} [Al] = 0.15 mol L^{-1} and [Na^+] = 1.31 mol L^{-1}, T = 25 °C. γ = 1%, ω = 4π rad s^{-1}.

first-order approximation for the gelation time of alumino-silicate hydrogels. We have indicated the formulation we study in detail by the dotted blue circle on the ternary diagram with a water content equal to 90% (Fig. 2).

3.2.2 Concentration dependencies. Gelation can occur between a few seconds and several hours, according to the reaction mixture. In order to highlight the impact of each chemical element on the time needed to reach a space-spanning percolated network, the gelation time t_{gel} was studied by varying independently the concentration of each component, [Si], [Al] and [Na], while maintaining the other concentrations at a constant. The resulting experimental values are shown in Fig. 4A–C for the variation of [Si], [Al] and [Na], respectively. In the first case, the concentrations of aluminate and sodium were fixed to 1.18 × 10^{-1} and 1.31 mol L^{-1} respectively and the silicate concentration was increased from 0.75 to 1.125 mol L^{-1} (Fig. 4A). Under these experimental conditions, the gelation time increases from 88 to 353 s.

The influence of aluminate was studied with [Na] fixed at 1.31 mol L^{-1} and two different concentrations of silicate: [Si] = 1.125 and 1.000 mol L^{-1} as shown by the red circle and blue triangle, respectively (Fig. 4B). For [Si] = 1.125 mol L^{-1}, increasing the aluminate concentration from 8.5× 10^{-2} to 2.12× 10^{-1} mol L^{-1} reduces t_{gel} from 617 to 108 s. Likewise, for [Si] = 1.000 mol L^{-1}, sweeping the aluminate concentration results in a decrease of t_{gel} from 402 to 70 s. Taken together, the results shown in Fig. 4A and B evidence that for a low Si/Al ratio, the gelation process is faster.

Fig. 4C shows that the gelation time decreases slightly when the sodium content is increased from 1.31 to 1.71 mol L^{-1}, regardless of the Si/Al ratio. The maximum concentration of sodium is restricted because values higher than 1.7–1.8 mol L^{-1} produce an inhomogeneous gel.

In our previous work, we highlighted that the gelation mechanism is related to the number of initial building blocks formed as a result of the polycondensation reaction between aluminates and silicate species.[16] The decrease of the Si/Al ratio – by increasing [Al] or decreasing [Si] – enables the formation of a higher number of initial building blocks in the reactive mixture. Increasing the volume fraction of building blocks leads to a decrease in the interparticle distance, favoring their interactions and consequently diminishing the gelation time and increasing the elastic modulus at the plateau (see Fig. S12 in the ESI†). On the other hand, increasing the sodium hydroxide concentration at a constant Si/Al ratio, increases the kinetic rate of gelation but the elasticity slightly decreases (see Fig. S12 in the ESI†). Those results are consistent with a decondensation process of the silicate oligomers by the hydroxide ions,[50] which makes these species more mobile and reactive with respect to polycondensation with aluminates. Additional SAXS/WAXS analyses and molecular simulation were also performed. Comparing the hydrogel and silicate solution scattering patterns highlighted that the measured signal originated from the silicate oligomers in the initial solution,[50] corresponding to the scattered signal of the homogeneous gel for $q > 0.1$ $Å^{-1}$.[72] These observations suggest that the stoichiometry of the gels is rapidly settled, with an excess of silicates suspended in the fluid phase.

3.2.3 Predicting variations in the gelation time according to the chemical formulation. The determination of the gelation time t_{gel} as a function of the chemical formulation allows us to propose an empirical law that can be described using the following equation which is represented by dashed lines in Fig. 4.

$$t_{gel} = k_{\theta,i} \times [i]^{\alpha_i} \quad (8)$$

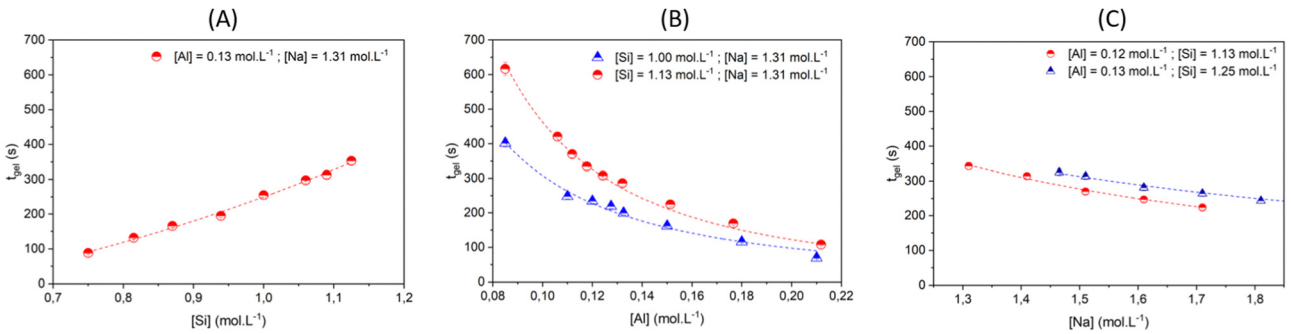

Fig. 4 Gelation time t_{gel} *vs.* concentration of (A) silicate, (B) aluminate and (C) sodium ions. Experimental data are represented by symbols. The model prediction, according to eqn (9) and data given in Table 1, are represented with dashed lines.

where $[i]$ is the concentration of element i (in mol L^{-1}), α_i is the partial order regarding the element i and $k_{\theta,i}$ is an associated constant which varies with absolute temperature θ (in K). The estimated error in the gelation time is approximately $t_{gel} \pm 3\%$ which is quite low but results from an average of three measurements. Considering each element involved in the condensation reactions and a given temperature, the previous expression can be generalized to the following form

$$t_{gel} = k_\theta \times \prod_i [i]^{\alpha_i} \quad (9)$$

where k_θ contains all of the partial rate constant $k_{\theta,i}$. Values of $k_{298.15K}$, α_{Si}, α_{Al} and α_{Na} were determined by regression of eqn (9) to all experimental data and are summarized in Table 1.

Some experiments were also performed for a few chemical formulations at three different temperatures. Interestingly, increasing the temperature (over a range $15 \leq \theta \leq 35°$) only accelerates the kinetics of gelation without modifying the viscoelastic moduli at the end of the reaction (see Fig. S5-A, ESI†).

Variation of the gelation time t_{gel} with temperature (see Fig. S5-B, ESI†) shows an Arrhenius relationship of the form: (10)

$$\frac{t_{gel}}{t_0} = \exp\left[\frac{E_a}{R}\left(\frac{1}{T} - \frac{1}{T_0}\right)\right] \quad (10)$$

where t_0 is the gelation time at a reference temperature T_0. This relationship suggests that ln t_{gel} increases with $1/T$ in a linear manner and the slope of such a plot is set by the ratio of the molar activation energy E_a over the universal gas constant R. By plotting $\ln(t_{gel})$ *versus* $1/T$ (see Fig. S5-B, ESI†) the activation energies E_a were calculated *via* linear regression to be 58.9 ± 3.5 kJ mol^{-1}. This is consistent with the aluminosilicate condensation process.[25]

The partial orders of the reaction listed in Table 1 will be discussed further below when we consider the aging process and the stoichiometry of the precipitated zeolite (Section 3.4.2.2).

3.3 Rheological behavior of the soft gel

3.3.1 Mechanical spectra. After formation of the hydrogels, we measured the corresponding viscoelastic spectra for various chemical compositions. Fig. 5A shows the increases in the elastic and loss moduli when the aluminum content of the initial reaction mixture increases. This behavior reflects the increasing volume fraction of amorphous solid particles in the gel. In each formulation, the storage modulus approaches a plateau at high frequency and the loss modulus shows a power law decrease with increasing frequency. The sudden upturn in $G''(\omega)$ at high frequency is associated with inertial effects in the controlled stress rheometer which scale with $I\omega^2$ (where I is the instrument inertia). This terminal behavior of the viscoelastic moduli at high frequencies indicates a decrease in the viscoelastic dissipation at shorter times and smaller length scales. The rheological behavior of all the mature aluminosilicate gels agree well with the theoretical predictions of the fractional Maxwell gel (FMG) model with a single constant value of the power low exponent α = 0.39. According to the parameters extracted from the FMG fits (presented in Fig. S6 of the ESI†), the experimental data can then be rescaled to construct the master curve shown in Fig. 5B.

The horizontal axis corresponds to the re-scaled dimensionless frequency $\omega\tau$, where τ is the characteristic relaxation time of the gel. The vertical axis shows the viscoelastic moduli scaled by the stiffness of the elastic network G_0. Finally, for this set of experimental data, the evolution of the three FMG parameters

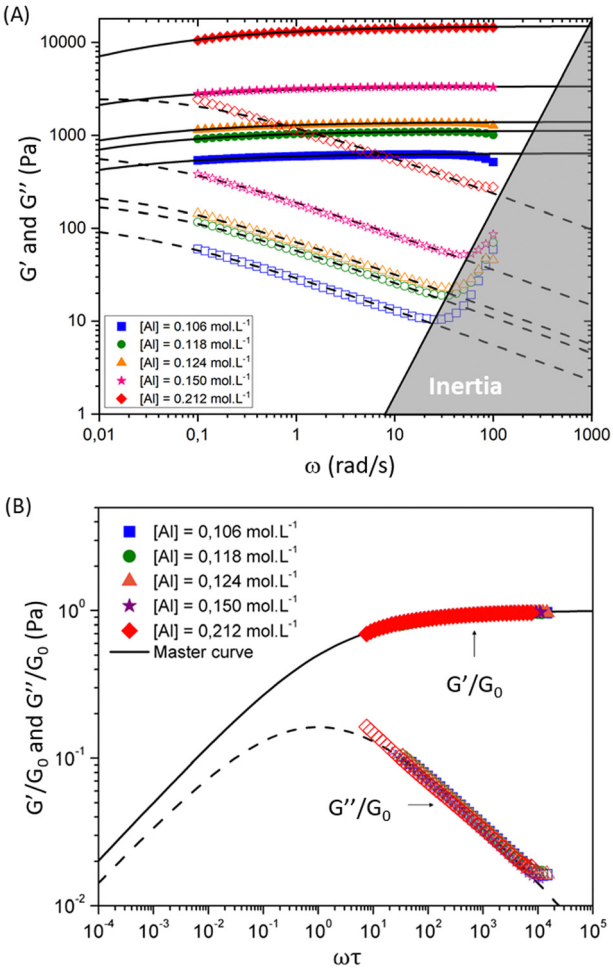

Fig. 5 Viscoelastic moduli for hydrogel samples with varying [Al] concentrations and fixed concentration of [Si] = 1.125 mol L^{-1} and [Na] = 1.31 mol L^{-1}. Filled and open symbols show the measured values of storage and loss moduli respectively. Solid and dashed lines show the fits of the FMG model (eqn (1) and (2)) for the storage and loss moduli respectively. The lower panel shows the dimensionless master curve for these samples. Dimensionless values of the reduced viscoelastic moduli G'/G_0 and G''/G_0 respectively are plotted as a function of the reduced frequency $\omega\tau$. Solid and dashed lines show fits to the dimensionless form of the FMG model (eqn (1) and (2)).

Table 1 Values of $k_{298.15K}$, α_{Si}, α_{Al} and α_{Na} determined from comparison of eqn (9) with experimental data

$k_{298.15K}$	α_{Si}	α_{Al}	α_{Na}
9.0	3.1	−1.7	−1.6

as a function of aluminum content are shown in Fig. S6 of the ESI.† The value of the power law exponent remains constant, indicating that the underlying percolation network, which is set at the gelation point, is geometrically self-similar between different chemical formulations in this set of samples. The two remaining fitting parameters (G_0, $\mathbb{V}$) evolve in a power-law manner with the [Al] concentration, suggesting that in these geometrically self-similar networks the corresponding scales for energy storage and dissipation and the associated time and length scales all evolve with increases in the effective volume fraction of particles.[55,56,73] The same behavior is observed for another two sets of experiments where the chemical formulations were changed. For a stoichiometrically unbalanced set (unbalanced means that before mixing of both solutions, the concentration of sodium is different in the silicate and aluminate solution. On the contrary for a stoichiometrically balanced set in which the silicate and aluminate solutions have the same concentration of sodium), the Al and Na content vary simultaneously, which consequently increases the value of the power law exponent $\alpha = 0.45$. The other model parameters evolve in a similar manner with [Al] concentration but exhibit different scaling exponents that are discussed later and in the ESI† (see Fig. S7–S11).

3.3.2 Yielding of the soft gels. To conclude the sequence of rheological tests, we perform a strain sweep until the gel exhibits non-linear behavior and ultimately fails at a large value of oscillatory strain, see Fig. 6. We estimate the end of the linear domain by a critical strain γ_c beyond which the storage modulus falls below 90% of the measured value at low strains. At larger strains, we observe a significant decrease in the measured values of viscoelastic moduli, and the material exhibits increasingly liquid-like behavior with values of the loss moduli being higher than storage moduli ($G'' > G'$). In can be seen from Fig. 6 that the critical strain γ_c decreases with increasing aluminum content and the corresponding increase in the volume fraction of amorphous solid entities.

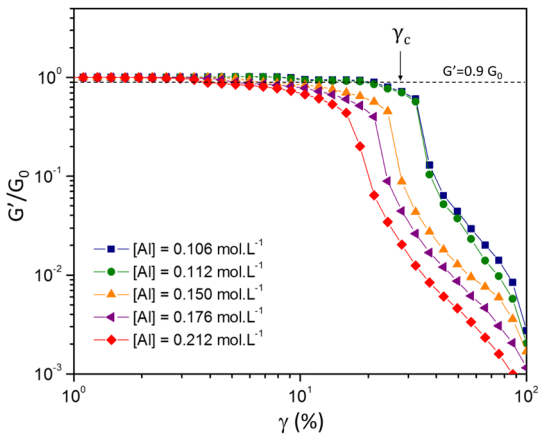

Fig. 6 Strain dependence of the elastic modulus G' normalized with the plateau modulus, G'/G_0, as a function of the imposed strain amplitude γ for various [Al] concentrations with [Si] = 1.125 mol L^{-1} and [Na] = 1.31 mol L^{-1}. We define γ_c as the critical strain when the elastic modulus reduces to $0.9G_0$.

3.3.3 Structure and compositional scaling of the aluminosilicate gel properties. As shown in Fig. 5 and 6, both the linear and nonlinear rheological properties of these gels evolve with increasing aluminum concentration. As summarized in Fig. 7, we clearly see that, by increasing the aluminum content, the elasticity of the mature gels also increases in a power-law manner $G_0 \propto [\mathrm{Al}]^{4.5}$, while the critical strain exhibits a decreasing power-law trend with $\gamma_c \propto [\mathrm{Al}]^{-2.25}$. To connect these power-law exponents to the underlying structure of the network, we rely on a model for elasticity of colloidal gels that was initially developed by Shih *et al.* and later extended by Wu *et al.*[55,56] The proposed model suggests a power-law scaling for the changes of elastic moduli and critical strains with increasing volume fraction:

$$G_0 \propto \phi^{\mu} \tag{11}$$

$$\gamma_c \propto \phi^{-\nu} \tag{12}$$

where μ and ν are power law exponents that are directly linked to intrinsic structural parameters such as the fractal dimension d_f, and backbone dimension x of the underlying network. We have assumed that the volume fraction is directly proportional to the aluminum concentration in our gels, which is also supported by calculation of Keshavarz *et al.*[16] in their ESI.†

Shih and coworkers[55] assumed that the structure of the mature gel is composed of fractal clusters that aggregate together and form a space-spanning network. Their proposed model considers two distinct regimes: the strong link regime, where the interfloc stiffness is greater than the intrafloc one, and the opposite regime, which is accordingly named the weak link regime. In the case of the strong link regime, the model predicts that for a network in 3D space the power-law exponents μ and ν are connected to structural parameters d_f and x *via* the

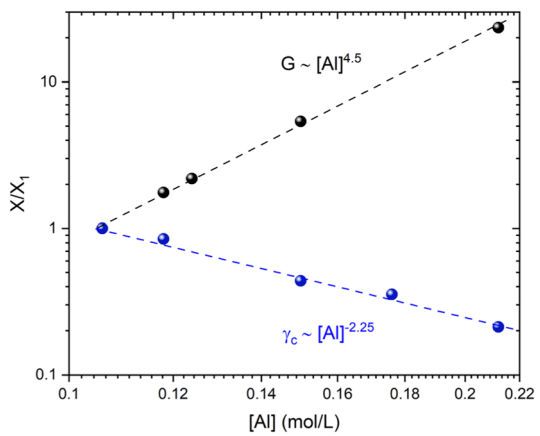

Fig. 7 Influence of the aluminum concentration on rheological properties. The normalized values (scaled with the value measured at [Al] = 0.106 mol L^{-1}) of the elastic moduli G_0/G_{0_i} and the critical strain γ_c/γ_{c_i} are determined from linear oscillatory tests and strain sweep experiments respectively. The measurements at $\omega = 1$ rad s^{-1} correspond to varying [Al] concentrations and a fixed composition of [Si] = 1.125 mol L^{-1} and [Na] = 1.31 mol L^{-1}.

relationships:

$$\mu = \frac{3 + x}{3 - d_f} \quad (13)$$

$$\nu = \frac{1 + x}{3 - d_f} \quad (14)$$

Replacing the power law exponent of μ = 4.5 and ν = 2.25 from Fig. 7, we can estimate values for cluster and backbone fractal dimensions d_f = 2.1 and x = 1.05 respectively. The estimated backbone fractal dimension x = 1.05 agrees well with the reported values in the literature for most colloidal gels.[55] We also determined the fractal dimension of the clusters separately from the scattering experiments on various gels. As shown in Fig. 8 and Table S1 of the ESI,† the USAXS/SAXS experimental results can be described by a composite model incorporating the fractal dimensions of the flocs and two length scales related to the size of the building blocks and of the clusters (see paragraph 10 in the ESI†). The model fits to the scattering data show that the cluster size and the length-scale of the building blocks vary systematically with the chemical formulation. However, the fractal dimension remains constant and equal to d_f = 2.1 (Table S1 in the ESI†) for all the tested chemical formulations that were produced with a fixed concentration of silicate ions and variable concentrations of aluminate and sodium ions. The same type of experiments and analysis was performed for other chemical formulations and the results are presented in the ESI,† file (Fig. S7–S9). When varying simultaneously the Na and Al concentrations, the scaling parameters decrease, suggesting a progressive modification of the intra- and inter-cluster links. However, the physical reasons for these variations are not fully understood yet and more studies are necessary to proceed further.

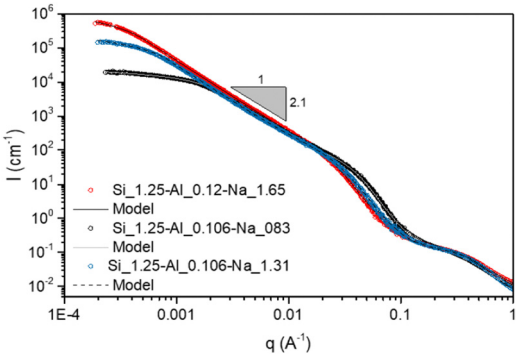

Fig. 8 USAXS data for aluminosilicate gels. The scattering data for the stoichiometrically balanced and unbalanced gels are shown with red and blue symbols respectively. Solid and dashed lines show fits from the scattering model (given in [Keshavarz *et al.*, *Proc. Natl. Acad. Sci. U. S. A.*, 2021, **118** (15), e2022339118] and in the ESI†). The fitting parameters are given in Table S1 of the ESI.†

3.4 Aging of the soft gel

3.4.1 Early aging: shrinkage of the gel and solvent release. Approximately one day after the formation of these soft aluminosilicate gels, a liquid film appeared at the top. The volume of supernatant increased rapidly with time, even at 25 °C. On the other hand, the crystallisation process and the precipitation of zeolites at room temperature are very long (the induction time is higher than one year). Consequently, it was decided to monitor the volumes occupied by the gel until the precipitation of zeolites by means of an accelerated aging method. Instead of applying a hydrothermal treatment to the gel where neither observations nor measurements over time can be carried out, the materials were directly formulated in transparent measuring cylinders at room temperature. After the gelling process was completed – at a time corresponding to the G' plateaus – each formulation was placed in an oven in airtight containers at either 40 °C or 50 °C in order to accelerate the precipitation of zeolites. Even in this case of moderate working temperatures the induction time, to visualize the transition between the homogeneous gel and the precipitation of crystals, is quite long. The slow pace of such a process with our chemical formulation, which starts from a homogeneous gel, is not yet fully understood. It is known that high alkalinity affects the crystallization kinetics drastically *via* variation in the Na_2O/SiO_2 ratio.[74] However, in their work, the authors studied the crystallization of zeolite A at room temperature and they found that precipitation occurs within three days. In our case, the Na_2O/SiO_2 and Al_2O_3/Na_2O ratios are ten times lower than the corresponding values in the mentioned study.[74] Similarly, we have used a much lower water content in our study. This can explain why we observe relatively long induction times at moderate working temperatures in our study. We could increase the temperature to shorten the time of precipitation but as we will see in the next section, the structure of zeolites will be affected at high temperatures. Moreover, a slower procedure enabled us to monitor the volume of the gel and the supernatant over time.

For various aluminum contents, the volume fraction occupied by the gel (in vol%) as a function of the aging time at 40 °C is plotted in Fig. 9A. For compositions ranging from [Al] = 0.106 to 0.177 mol L^{-1}, the volume fraction of the gel slightly decreases during the first five days, until a stable local plateau value is reached. Then, the volume fraction remains constant for more than 50 days. The volume fraction of the gel at the plateau depends of the formulation and decreases with increasing aluminate content. At the highest concentration of [Al] = 0.212 mol L^{-1}, no intermediate plateau was observed and the volume fraction of the gel slowly but continuously decreased during the aging process. However, varying the sodium content did not seem to have an influence on the volume fraction of the shrunken gel obtained (Fig. S13 of the ESI†). Regardless of the Na concentration, the shrunken gel occupied 97 vol% of the total volume.

The observation of a clear supernatant solution exuded from the gel is a typical sign of a syneretic phenomenon. As pointed out by Scherer,[75] syneresis in inorganic gels is generally attributed to condensation reactions that cause a progressive contraction of the solid phase, squeezing the liquid phase out of the gel. However, the role of this phenomenon in the

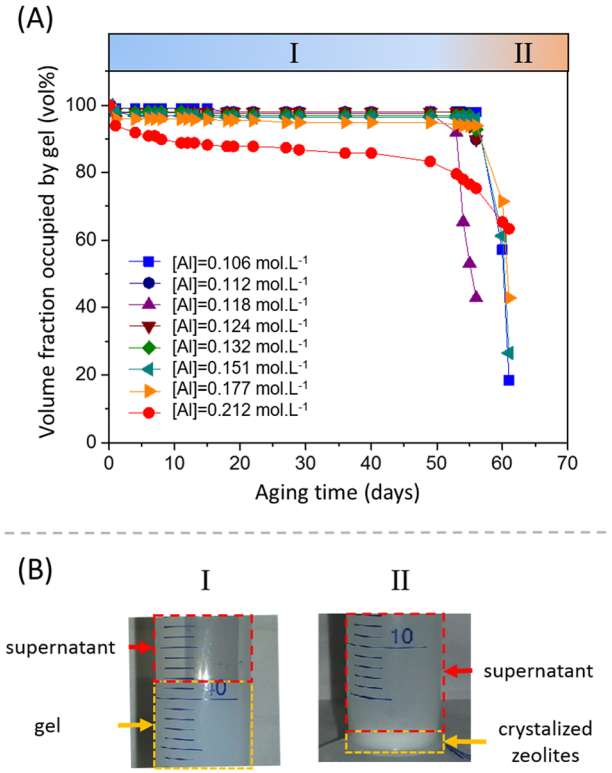

Fig. 9 (A) Volume fraction of hydrogel (vol%) *vs.* aging time (days) at 40 °C; (B) photos of the two time scales of evolution I; shrinking of hydrogel and expulsion of the excess solution (day 7) and II: destabilization and sedimentation of a solid precipitate (day 65). [Si] = 1.125 mol L^{-1} and [Na] = 1.31 mol L^{-1}.

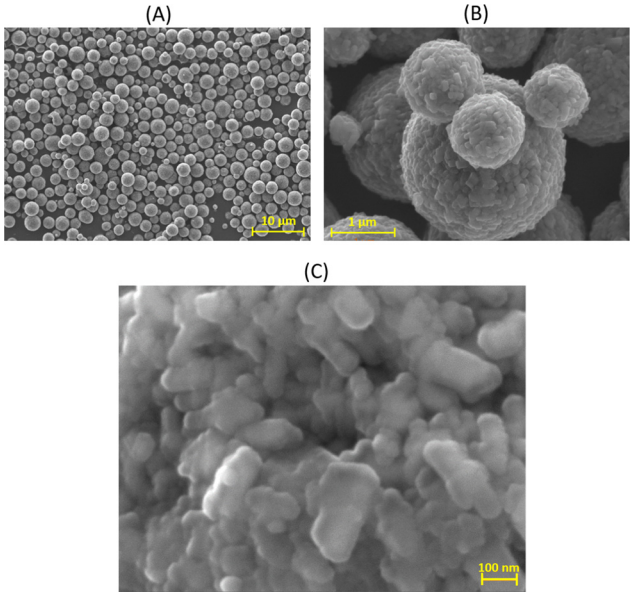

Fig. 10 HR-SEM pictures of zeolite obtained after 60 days of aging at 40 °C, for a gel formulated with the following concentrations: [Si] = 1.125 mol L^{-1}; [Al] = 0.118 mol L^{-1} and [Na] = 1.31 mol L^{-1}. Magnifications: 2000× (A), 25 000× (B) and 100 000× (C).

precipitation of zeolites has not been reported in the literature. Itani *et al.*[31] discussed the important role of sodium hydroxide on the zeolite microstructure and on the precipitation rate but do not address the effect of syneresis. This is not entirely surprising, because zeolites are often synthesised from hydrogels in an autoclave, meaning that a lot of amorphous aluminosilicate species are present in the system and suspended in the liquid phase but without any mechanical strength, rendering visualization of the water flux difficult. The release of liquid by syneresis causes a gradual shrinkage and de-watering of the gel, which is consistent with the slow decrease of the viscous modulus G'' observed in Fig. 3 for $t > 1000$ s.

3.4.2 Long time aging: gel destabilization and zeolite precipitation

3.4.2.1 Morphology. At longer aging time (>50 days), a fast destructuration of the gel is observed (region II of Fig. 9A). The volume fraction occupied by the gel phase drops to values around 20–40% in 1 or 2 days, and the system becomes an inhomogeneous mixture composed of solid white precipitates and an amorphous gel. The nucleation and growth of zeolites starts and, at the end of the process, we observe a sediment layer of white particles at the bottom of the tube (see Fig. 9B.II). These particles were filtered, dried at 200 °C and characterized by HR-SEM, which showed that the zeolitic particles have a typical spherical shape, with a diameter of 1–2 µm (Fig. 10A). The zeolites are composed of aggregated nano-particles, with individual diameters around 100–200 nm (Fig. 10B and C). A similar microstructure was observed by Kumar *et al.*[76] for SSZ-13 chabazite-type aluminosilicate zeolite. As these authors suggest, crystallization by particle attachment[52] seems to be the dominant mechanism, leading to the formation of spheroidal, highly roughened crystals. The size of the nano-grains is consistent with the scattering data obtained on the amorphous gels (Fig. 8 and Table S3 of the ESI†), from which a radius of gyration around 150 nm was determined. As suggested in our previous paper,[16] the space-filling structure formed right at the gel point of the amorphous gel is close to the structure of the solid particles and this is confirmed by the direct microscopic observation of the zeolites.

3.4.2.2 Zeolite characterization. The elemental composition of the particles (in terms of stoichiometry) was estimated by measuring the Si, Al and Na concentrations, before the gelation and after the destabilization of the gel, for the various formulations. The concentration differences Δ[Al], Δ[Si] and Δ[Na] were calculated from the initial concentrations $[i]_{ini}$ and the equilibrium concentrations $[i]_{eq}$ measured in the supernatant after denaturation of the gel ($\Delta[i] = [i]_{ini} - [i]_{eq}$). These changes Δ[Al] and Δ[Si] are shown as a function of the aluminum concentration in Fig. 11. These differences correspond to the amounts of aluminum and silicon that react to form the precipitated material. The change in Δ[Na] is not shown because the data perfectly overlay with the Δ[Al] data. Regardless of the temperature of the aging experiments, the changes in Δ[Al] (and Δ[Na]) and Δ[Si] increase with increasing the initial concentration $[Al]_{ini}$. The aging temperature has no significant influence on Δ[Al] (or Δ[Na]) and Δ[Si] evolutions. The slopes of these

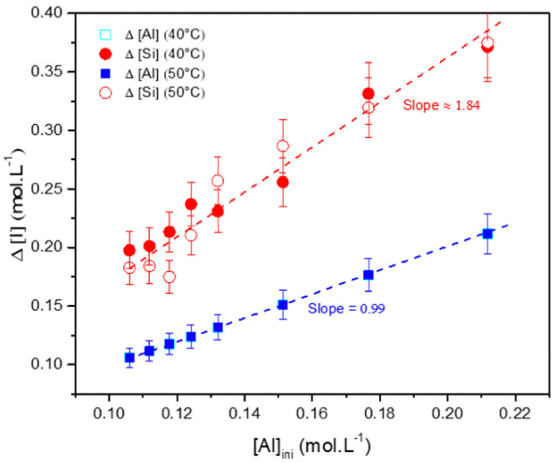

Fig. 11 Change in the concentration of Δ[Si] and Δ[Al] as a function of the initial concentration of aluminate $[Al]_{ini}$ after aging at 40° or 50°. $\Delta[i] = [i]_{ini} - [i]_{eq}$. Gel formulation: [Si] = 1.125 mol L^{-1}; [Al] = 0.118 mol L^{-1} and [Na] = 1.31 mol L^{-1}.

changes in ion concentrations Δ[Al] (or Δ[Na]) and Δ[Si] are shown on the plot and equal to 0.99 (or 0.99) and 1.84, respectively. Thus, the change in Δ[Al] appears to be equal to $[Al]_{ini}$, meaning that the aluminates entirely react with silicates. The two-fold increase in the slope for Δ[Si] results suggest that two silicates react with one aluminate. The sodium follows the aluminum concentration, meaning that charge compensation takes place in the gel.

Furthermore, XRD patterns of the recovered powder highlighted primarily a chabazite-type structure, regardless of the concentration of aluminum or sodium, with the chemical formula: $Na_2Al_2Si_4O_{12}{\cdot}6H_2O$ (Fig. 12 and Fig. S14 and S15 in the ESI†). For the aging experiments at 50 °C, a similar microstructure is observed but the composition is a mixture of chabazite, faujasite and gmelinite (Fig. S16 and S17 in the ESI†). These crystals correspond to other zeolites with different numbers of water hydration molecules in their crystalline structures ($Na_2Al_2Si_4O_{12}{\cdot}nH_2O$, see the ESI†). Nevertheless, the

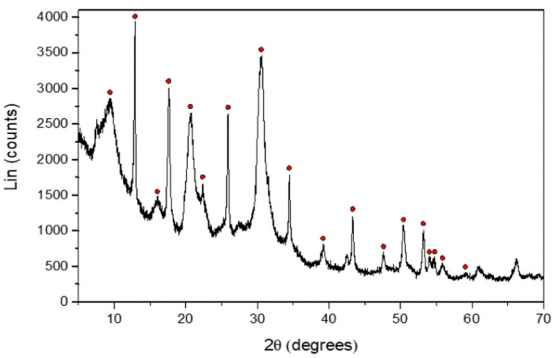

Fig. 12 XRD pattern of chabazite-type zeolite, obtained after 60 days of aging at 40 °C. The concentration of the chemical elements constituting the gel is: [Si] = 1.125 mol L^{-1}; [Al] = 0.118 mol L^{-1} and [Na] = 1.31 mol L^{-1}. Red points correspond to the Chabazite-type structure ($Na_2Al_2Si_4O_{12}{\cdot}6H_2O$).

stoichiometry of the precipitated zeolite (two Si atoms for each Al atom) is very close to the ratio Δ[Si]/Δ[Al] of the remaining chemicals in the solution (∼1.84). Moreover, one should note that Δ[Si]/Δ[Al] ∼ 1.84 (Fig. 11), which is also consistent with the ratio of the chemical elements partial orders $|\alpha_{Si}/\alpha_{Al}| \sim 1.82$ (Table 1) determined by means of eqn (9). Similarly, the $|\alpha_{Na}/\alpha_{Al}|$ ratio is determined to be equal to 0.94, which is very similar to the ratio found in the supernatant (Δ[Na]/Δ[Al]) or in the zeolite, meaning that the cation compensates the negative charge of the aluminum in the amorphous or zeolite framework. This result, which needs further independent investigation, suggests that the zeolite stoichiometry is determined at the early stages of gelation ($t \ll t_{gel}$), *i.e.* the discrete aluminosilicate building blocks are initially formed to establish the native structure of the gel network. When combined with our earlier study of these systems,[16] we now have a number of convergent observations pointing at the strong correlation between the morphology and the texture of the amorphous gel network that is initially established at short times (on the order of t_{gel}) and of the precipitated crystals obtained on much longer time scales (dependent on the aging temperature).

4 Conclusions

Monolithic optically clear homogeneous aluminosilicate gels were investigated in alkali solutions and characterized from their early age to the final crystallisation of zeolites. We first identified the range of chemical compositions that allow generation of a homogeneous hydrogel, through the determination of ternary diagrams for four different levels of water contents (given by the ratio $m(H_2O)/\sum m(i)$). The importance of the gel preparation (the concentration of each constituent, the mixing temperature and even the balance of the concentrations in the two solutions before mixing) was determined in order to avoid production of inhomogeneous gels. After identification of the homogeneous zone in the ternary diagram, the influence of the molar concentration of each constituent (Al, Si and Na) was studied, through systematic variation of each component, from kinetic, rheological and structural points of view as well as through consideration of the syneretic aging process. The rate of gelation and the evolution on the viscoelastic properties over a range of temperatures were then investigated through a multiparametric study, allowing us to deconvolve the effect of each chemical element involved in the overall gelation reaction. We determined that the time to gelation is faster at high temperature and follows an Arrhenius law with an activation energy of $E_a = 64 \pm 10$ kJ mol^{-1}. The gelation time t_{gel}, determined from the crossover between the elastic G' and the viscous G'' contributions to the complex modulus, could be modeled using an empirical rate law and the partial orders of the hydrogel reaction ($\alpha_{Si} = 3.1$, $\alpha_{Al} = -1.7$ and $\alpha_{Na} = -1.6$) were derived.

Measurement of the viscoelastic spectra of the mature gels reveals the influence of each chemical element, especially the aluminum and sodium cations, which play the role of

bond-maker and bond-breaker respectively. The frequency dependency of the viscoelastic moduli are self-similar and have a number of common characteristics regardless of the chemical formulation. There is a clear plateau modulus at high frequencies in the elastic response and a power law decrease in the loss modulus. These frequency-dependent responses are also well described by the theoretical predictions of a very simple three parameter (α, $\mathbb{V}$ and G_0) Fractional Maxwell Gel Model (FMG). The structural parameter of the model, α, characterizing the frequency dependence of the viscoelastic spectrum is very well correlated to the fractal dimension measured in these gels by USAXS as discussed elsewhere.[16] Indeed, Muthukumar[77] has suggested that the structural parameter d_f, namely the fractal dimension of the underlying network, can be connected to the relaxation exponent α in fractional models $\alpha = 3(5 - 2d_f)/2(5 - d_f)$. Using the values of the fitted model parameters, particularly the elastic modulus G_0 and the relaxation time τ of the gel (calculated from the three model parameters *via* the relationship $\tau = (\mathbb{V}/G_0)^{1/\alpha}$), all the mechanical spectra can be scaled onto a master curve by using the elasticity and the relaxation time as vertical and horizontal shifting parameters respectively.

By studying the yielding of the gels at larger deformation amplitudes, the Shih *et al.*[55] model could be applied to two distinct sets of chemical formulations. This model is ideally suited for describing our fractal colloidal gels that have aggregated according to a Reaction Limited Cluster Aggregation (RLCA) mechanism. By carefully observing the evolution of the gel elastic modulus and the critical strain for yielding the gels as a function of the aluminum content (keeping Si and Na constant), we obtain distinctive positive and negative power law scaling exponents respectively. These exponents are consistent with the strong-link regime described by Shih *et al.*[55] and are consistent with the values of the fractal dimension of the clusters obtained at the mesoscale by USAXS. This strong-link behavior indicates that the interfloc stiffness is stronger than the intrafloc connections. By modifying the chemical formulation, especially the sodium content, we are able to decrease the two power-law exponents and tune the mechanical properties until the stiffness of the connections between the flocs and within each individual flocs starts to become comparable.

Our study of the characteristics of these gels aging showed that at early times the gelled structures exhibit shrinkage concomitant with the release of liquid at the surface due to syneresis. At longer times a destabilization of the hydrogel occurs between 20 days and several months, depending on the temperature storage. This destabilization is due to the *in situ* crystallization of zeolites as chabazite or other zeolitic structural forms, depending on the aging temperature. Electron microscopy shows the precipitated zeolitic particles are composed of aggregated nano-particles, suggesting a mechanism of precipitation by crystallized particle attachment.

Finally, we note that the stoichiometry of the precipitated zeolites is not only consistent with the residual concentration of the supernatant but surprisingly, it is also very close to the partial order of reaction of the chemical elements determined by rheological measurements in the neighborhood of the critical gel point. This suggests a strong correlation between (i) the rheomechanical properties and fractal structural characteristics of the initial amorphous gel network established at the instant of gelation, and (ii) the final precipitated crystals.

Data availability

Please note that the data supporting this article have been included as part of the ESI.†

Conflicts of interest

There are no conflicts to declare.

Acknowledgements

The authors acknowledge The French National Research Agency (ANR) for financial support of the DYNAMISTE project (ANR-15-CE07-0013). The authors want to thank Olivier Grauby from Cinam Marseille and Pascal Antonucci from the CEA, DES, ISEC, DPME for their assistance for HRSEM and XRD, respectively. The authors also wish to acknowledge the MISTI-France program for promoting collaborative research and exchange.

Notes and references

1 M. E. Davis, *Nature*, 2002, **417**, 813–821.
2 Y. Li and J. Yu, *Nat. Rev. Mater.*, 2021, **6**, 1156–1174.
3 P. Duxson, A. Fernández-Jiménez, J. L. Provis, G. C. Lukey, A. Palomo and J. S. J. van Deventer, *J. Mater. Sci.*, 2007, **42**, 2917–2933.
4 Z. Zhang, J. L. Provis, A. Reid and H. Wang, *Constr. Build. Mater.*, 2014, **56**, 113–127.
5 S. Wang and Y. Peng, *Chem. Eng. J.*, 2010, **156**, 11–24.
6 R. P. Townsend and E. N. Coker, *Studies in Surface Science and Catalysis*, Elsevier, 2001, vol. 137, pp. 467–524.
7 W. Zhang, S. Li, J. Wei, Q. Zhang, R. Liu, X. Zhang and H. Yin, *Carbonates Evaporites*, 2018, **33**, 211–222.
8 S. Kazemian and A. Prasad, *Grouting and Deep Mixing 2012*, New Orleans, Louisiana, United States, 2012, pp. 1701–1710.
9 V. Cantarel, F. Nouaille, A. Rooses, D. Lambertin, A. Poulesquen and F. Frizon, *J. Nucl. Mater.*, 2015, **464**, 16–19.
10 S. Petlitckaia, Y. Barré, T. Piallat, O. Grauby, D. Ferry and A. Poulesquen, *J. Cleaner Prod.*, 2020, **269**, 122400.
11 A. Rooses, P. Steins, A. Dannoux-Papin, D. Lambertin, A. Poulesquen and F. Frizon, *Appl. Clay Sci.*, 2013, **73**, 86–92.
12 L. Frances, M. Douilly, M. Grivet, D. Ducret and M. Théobald, *J. Phys. Chem. C*, 2015, **119**, 28462–28469.
13 T. Hijikata, T. Koyama, Y. Aikyo, S. Shimura and M. Kawanishi, *J. Nuclear Sci. Technol.*, 2021, **58**, 1079–1098.
14 J. Davidovits, *J. Therm. Anal. Calorim.*, 1991, **37**, 1633–1656.
15 J. Aupoil, J.-B. Champenois, J.-B. d'Espinose de Lacaillerie and A. Poulesquen, *Cem. Concr. Res.*, 2019, **115**, 426–432.

16 B. Keshavarz, D. G. Rodrigues, J.-B. Champenois, M. G. Frith, J. Ilavsky, M. Geri, T. Divoux, G. H. McKinley and A. Poulesquen, *Proc. Natl. Acad. Sci. U. S. A.*, 2021, **118**, e2022339118.
17 P. Steins, A. Poulesquen, O. Diat and F. Frizon, *Langmuir*, 2012, **28**, 8502–8510.
18 M. F. Alnahhal, T. Kim and A. Hajimohammadi, *Cem. Concr. Res.*, 2021, **144**, 106441.
19 X. Dai, S. Aydn, M. Y. Yardmc, K. Lesage and G. De Schutter, *Cem. Concr. Res.*, 2020, **138**, 106253.
20 I. Krznarić, T. Antonić and B. Subotić, *Zeolites*, 1997, **19**, 29–40.
21 V. Valtchev and L. Tosheva, *Chem. Rev.*, 2013, **113**, 6734–6760.
22 P. Rożek, M. Król and W. Mozgawa, *J. Cleaner Prod.*, 2019, **230**, 557–579.
23 P. Steins, A. Poulesquen, O. Diat and F. Frizon, *Langmuir*, 2012, **28**, 8502–8510.
24 J. L. Bell, P. Sarin, J. L. Provis, R. P. Haggerty, P. E. Driemeyer, P. J. Chupas, J. S. J. van Deventer and W. M. Kriven, *Chem. Mater.*, 2008, **20**, 4768–4776.
25 A. Poulesquen, F. Frizon and D. Lambertin, *J. Non-Cryst. Solids*, 2011, **357**, 3565–3571.
26 J. Rouyer and A. Poulesquen, *J. Am. Ceram. Soc.*, 2015, **98**, 1580–1587.
27 J. W. Phair, J. C. Schulz, L. P. Aldridge and J. D. Smith, *J. Am. Ceram. Soc.*, 2004, **87**, 129–137.
28 J. Mills, P. Mondal and N. J. Wagner, *Cem. Concr. Res.*, 2022, **151**, 106618.
29 S. Yu, S. Kwon and K. Na, *J. Sol-Gel Sci. Technol.*, 2021, **98**, 411–421.
30 H. Shen, H. Maekawa, J. Kawamura, Y. Matsumoto, T. Yamamura, Y. Kawakita, K. Shibata and M. Kawai, *Solid State Ionics 16: Proceedings of the 16th International Conference on Solid State Ionics (SSI-16), Part I*, 2008, vol. 179, pp. 1133–1137.
31 L. Itani, Y. Liu, W. Zhang, K. N. Bozhilov, L. Delmotte and V. Valtchev, *J. Am. Chem. Soc.*, 2009, **131**, 10127–10139.
32 S. Mintova, N. H. Olson, V. Valtchev and T. Bein, *Science*, 1999, **283**, 958–960.
33 V. P. Valtchev and K. N. Bozhilov, *J. Am. Chem. Soc.*, 2005, **127**, 16171–16177.
34 C. Kosanović, S. Bosnar, B. Subotić, V. Svetličić, T. Mišić, G. Dražić and K. Havancsák, *Microporous Mesoporous Mater.*, 2008, **110**, 177–185.
35 C. Kosanović, S. Bosnar, B. Subotić, V. Svetličić, T. Mišić, G. Dražić and K. Havancsák, *Microporous Mesoporous Mater.*, 2008, **110**, 177–185.
36 A. I. Lupulescu and J. D. Rimer, *Science*, 2014, **344**, 729–732.
37 P.-P. E. A. de Moor, T. P. M. Beelen, R. A. van Santen, K. Tsuji and M. E. Davis, *Chem. Mater.*, 1999, **11**, 36–43.
38 M. Ogura, Y. Kawazu, H. Takahashi and T. Okubo, *Chem. Mater.*, 2003, **15**, 2661–2667.
39 M. Smaihi, O. Barida and V. Valtchev, *Eur. J. Inorg. Chem.*, 2003, 4370–4377.
40 A. Aerts, L. R. A. Follens, E. Biermans, S. Bals, G. Van Tendeloo, B. Loppinet, C. E. A. Kirschhock and J. A. Martens, *Phys. Chem. Chem. Phys.*, 2011, **13**, 4318.
41 X. Zhao, R. Liu, H. Zhang, Y. Shang, Y. Song, C. Liu, T. Wang, Y. Gong and Z. Li, *J. Appl. Crystallogr.*, 2017, **50**, 231–239.
42 T. M. Davis, T. O. Drews, H. Ramanan, C. He, J. Dong, H. Schnablegger, M. A. Katsoulakis, E. Kokkoli, A. V. McCormick, R. L. Penn and M. Tsapatsis, *Nat. Mater.*, 2006, **5**, 400–408.
43 W. Fan, M. Ogura, G. Sankar and T. Okubo, *Chem. Mater.*, 2007, **19**, 1906–1917.
44 W. H. Dokter, H. F. van Garderen, T. P. M. Beelen, R. A. van Santen and W. Bras, *Angew. Chem., Int. Ed. Engl.*, 1995, **34**, 73–75.
45 M. D. Oleksiak and J. D. Rimer, *Rev. Chem. Eng.*, 2014, **30**, 1–49.
46 N. Ren, B. Subotić, J. Bronić, Y. Tang, M. Dutour Sikirić, T. Mišić, V. Svetličić, S. Bosnar and T. Antonić Jelić, *Chem. Mater.*, 2012, **24**, 1726–1737.
47 M. Kumar, R. Li and J. D. Rimer, *Chem. Mater.*, 2016, **28**, 1714–1727.
48 R. Li, A. Chawla, N. Linares, J. G. Sutjianto, K. W. Chapman, J. G. Martínez and J. D. Rimer, *Ind. Eng. Chem. Res.*, 2018, **57**, 8460–8471.
49 J. Aupoil, J.-B. Champenois, J.-B. d'Espinose de Lacaillerie and A. Poulesquen, *Cem. Concr. Res.*, 2019, **115**, 426–432.
50 R. Dupuis, D. Gomes Rodrigues, J.-B. Champenois, R. J.-M. Pellenq and A. Poulesquen, *J. Phys.: Mater.*, 2020, **3**, 014012.
51 R. Jain, A. J. Mallette and J. D. Rimer, *J. Am. Chem. Soc.*, 2021, **143**, 21446–21460.
52 J. J. De Yoreo, P. U. P. A. Gilbert, N. A. J. M. Sommerdijk, R. L. Penn, S. Whitelam, D. Joester, H. Zhang, J. D. Rimer, A. Navrotsky, J. F. Banfield, A. F. Wallace, F. M. Michel, F. C. Meldrum, H. Colfen and P. M. Dove, *Science*, 2015, **349**, aaa6760.
53 E. Zaccarelli, *J. Phys.: Condens. Matter*, 2007, **19**, 323101.
54 M. Y. Lin, H. M. Lindsay, D. A. Weitz, R. C. Ball, R. Klein and P. Meakin, *Phys. Rev. A: At., Mol., Opt. Phys.*, 1990, **41**, 2005–2020.
55 W.-H. Shih, W. Y. Shih, S.-I. Kim, J. Liu and I. A. Aksay, *Phys. Rev. A: At., Mol., Opt. Phys.*, 1990, **42**, 4772–4779.
56 H. Wu and M. Morbidelli, *Langmuir*, 2001, **17**, 1030–1036.
57 M. Geri, B. Keshavarz, T. Divoux, C. Clasen, D. J. Curtis and G. H. McKinley, *Phys. Rev. X*, 2018, **8**, 041042.
58 J. D. J. Rathinaraj, G. H. McKinley and B. Keshavarz, *Fractal Fractional*, 2021, **5**, 174.
59 J. E. Martin and D. Adolf, *Annu. Rev. Phys. Chem.*, 1991, **42**, 311–339.
60 A. Jaishankar and G. H. McKinley, *Proc. R. Soc. London, Ser. A*, 2013, **469**, 20120284.
61 H. H. Winter and F. Chambon, *J. Rheology*, 1986, **30**, 367–382.
62 J. Ilavsky, F. Zhang, A. J. Allen, L. E. Levine, P. R. Jemian and G. G. Long, *Metall. Mater. Trans. A*, 2013, **44**, 68–76.
63 J. Ilavsky, F. Zhang, R. N. Andrews, I. Kuzmenko, P. R. Jemian, L. E. Levine and A. J. Allen, *J. Appl. Crystallogr.*, 2018, **51**, 867–882.

64 J. Ilavsky, *J. Appl. Crystallogr.*, 2012, **45**, 324–328.
65 J. Ilavsky and P. R. Jemian, *J. Appl. Crystallogr.*, 2009, **42**, 347–353.
66 A. Palčić, B. Subotić, V. Valtchev and J. Bronić, *CrystEngComm*, 2013, **15**, 5784.
67 S. D. Kinrade and T. W. Swaddle, *Inorg. Chem.*, 1988, **27**, 4253–4259.
68 I. L. Svensson, S. Sjöberg and L.-O. Öhman, *J. Chem. Soc., Faraday Trans. 1*, 1986, **82**, 3635.
69 C. J. Brinker and G. W. Scherer, *Sol-Gel Science: The Physics and Chemistry of Sol-Gel Processing*, Elsevier, 1990.
70 J. Šefcík and A. McCormick, *Microporous Mater.*, 1997, **10**, 173–179.
71 S. M. Fielding, P. Sollich and M. E. Cates, *J. Rheology*, 2000, **44**, 323–369.
72 R. Dupuis, S. H. Hahn, A. C. T. van Duin, R. J.-M. Pellenq and A. Poulesquen, *Phys. Chem. Chem. Phys.*, 2022, **24**, 9229–9235.
73 R. Buscall, P. D. A. Mills, J. W. Goodwin and D. W. Lawson, *J. Chem. Soc., Faraday Trans. 1*, 1988, **84**, 4249.
74 V. P. Valtchev, L. Tosheva and K. N. Bozhilov, *Langmuir*, 2005, **21**, 10724–10729.
75 G. W. Scherer, *J. Non-Cryst. Solids*, 1989, **108**, 18–27.
76 M. Kumar, H. Luo, Y. Román-Leshkov and J. D. Rimer, *J. Am. Chem. Soc.*, 2015, **137**, 13007–13017.
77 M. Muthukumar, *Macromolecules*, 1989, **22**, 4656–4658.

